Realignment and suppression of charge density waves in the rare-earth tritellurides $R\mathrm{Te}_3$ (R = La, Gd, Er)

Saif Siddique,[1] James L. Hart,[1] Drake Niedzielski,[2] Ratnadwip Singha,[3,4] Myung-Geun Han,[5] Stephen D. Funni,[1] Michael Colletta,[6] Mehrdad T. Kiani,[1] Noah Schnitzer,[1] Natalie L. Williams,[7] Lena F. Kourkoutis,[6] Yimei Zhu,[5] Leslie M. Schoop,[3] Tomás A. Arias,[2] and Judy J. Cha[1]

[1]*Department of Materials Science and Engineering, Cornell University, Ithaca, New York 14853, USA*
[2]*Department of Physics, Cornell University, Ithaca, New York 14853, USA*
[3]*Department of Chemistry, Princeton University, Princeton, New Jersey 08544, USA*
[4]*Department of Physics, Indian Institute of Technology Guwahati, Assam 781039, India*
[5]*Condensed Matter Physics and Materials Science Department, Brookhaven National Laboratory, Upton, New York 11973, USA*
[6]*School of Applied and Engineering Physics, Cornell University, Ithaca, New York 14853, USA*
[7]*Department of Chemistry, Cornell University, Ithaca, New York 14853, USA*

(Received 9 April 2024; revised 25 June 2024; accepted 12 July 2024; published 25 July 2024)

The rare-earth tritellurides have a rich phase diagram that includes charge density waves (CDWs), superconductivity, and magnetic order, offering a platform to study the interplay between these phases on a square-net system. Prior studies have shown that defects can affect the CDW characteristics in these materials, yet coupling between the CDW order and the underlying microstructure has not been studied at the nanoscale. Here we use scanning transmission electron microscopy at cryogenic temperatures to directly visualize the effects of defects on the CDW order and provide a spatially resolved microscopic correlation between the CDW transition and structural defects. We show that in the presence of extended defects, such as dislocations and stacking faults, the weak orthorhombicity of the rare-earth tritellurides is lost and the material becomes pseudotetragonal. Since the orthorhombicity acts as a symmetry breaking field for the CDW transitions in rare-earth tritellurides, the presence of these extended defects modulates the energetics of the CDWs and suppresses the ground-state CDW phase at low temperature.

DOI: 10.1103/PhysRevB.110.014111

I. INTRODUCTION

Crystal defects like dislocations and stacking faults are imperfections that disrupt periodic order in crystalline solids. Their presence shapes many mechanical and electronic properties of materials [1–4]. In charge density wave (CDW) systems, the perturbation potential from these defects can affect the critical parameters and properties of CDWs and lead to the formation of CDW pinning sites, emergence of incommensurate domains, and suppression of the CDW amplitude [5–10]. Since electron-phonon coupling is strong in CDW systems [11,12], lattice distortions from defects will influence the CDW phases, necessitating detailed microscopic studies to link the CDW behavior with the underlying structural defects. However, techniques that allow a direct characterization of defect-CDW interactions are limited. Scanning tunneling microscopy is commonly used for atomic-scale characterization, but it is strictly surface sensitive with a limited field of view, and thus often unable to access complete defect structures, especially for extended defects like dislocations. Other techniques like x-ray or neutron diffraction and optical measurements are either indirect probes or lack sufficient spatial resolution. In contrast, transmission electron microscopy (TEM) provides a nanoscale spatial resolution and thickness-averaged structural information, as evidenced by prior CDW studies [13–15]. Further, *in situ* cryogenic scanning TEM (cryo-STEM) can access and control relevant temperatures and length scales, enabling direct correlation of microstructural features with local CDW order in real space. In this work, we study the defect-CDW coupling in rare-earth tritellurides ($R\mathrm{Te}_3$; R = La, Gd, and Er) using *in situ* cryo-STEM.

$R\mathrm{Te}_3$ materials are layered, quasi-two-dimensional (2D) compounds with multiple CDW orders [11,16–18], including at least one unconventional CDW phase exhibiting an axial Higgs mode [19]. Due to lanthanide contraction, the size of the rare-earth elements decreases along the Periodic Table and results in tunable CDW behavior as a function of R. $R\mathrm{Te}_3$'s with larger rare-earth elements (La-Gd) have a unidirectional, incommensurate CDW (CDW_1), while $R\mathrm{Te}_3$'s with smaller rare-earth elements (Tb-Tm) have an additional incommensurate CDW (CDW_2) at a lower temperature, orthogonal to CDW_1, creating a bidirectional CDW state [17,20]. $R\mathrm{Te}_3$'s belong to the orthorhombic space group *Cmcm* with the presence of a **c** glide (glide plane perpendicular to the **b** axis and glide direction along the **c** axis) [Fig. 1(a)]. The unit cell consists of two layers of $R\mathrm{Te}_3$, where each layer comprises a corrugated R-Te block sandwiched between square nets of Te. The two in-plane lattice parameters differ slightly with $|\boldsymbol{a}| < |\boldsymbol{c}|$ by ∼0.2 pm [21]. This weak anisotropy between the **a** and **c** axes couples with the CDWs in these materials, and the high-temperature CDW_1 preferentially orients along the **c** axis in the Te square net. Straquadine *et al.*

 ©2024 American Physical Society

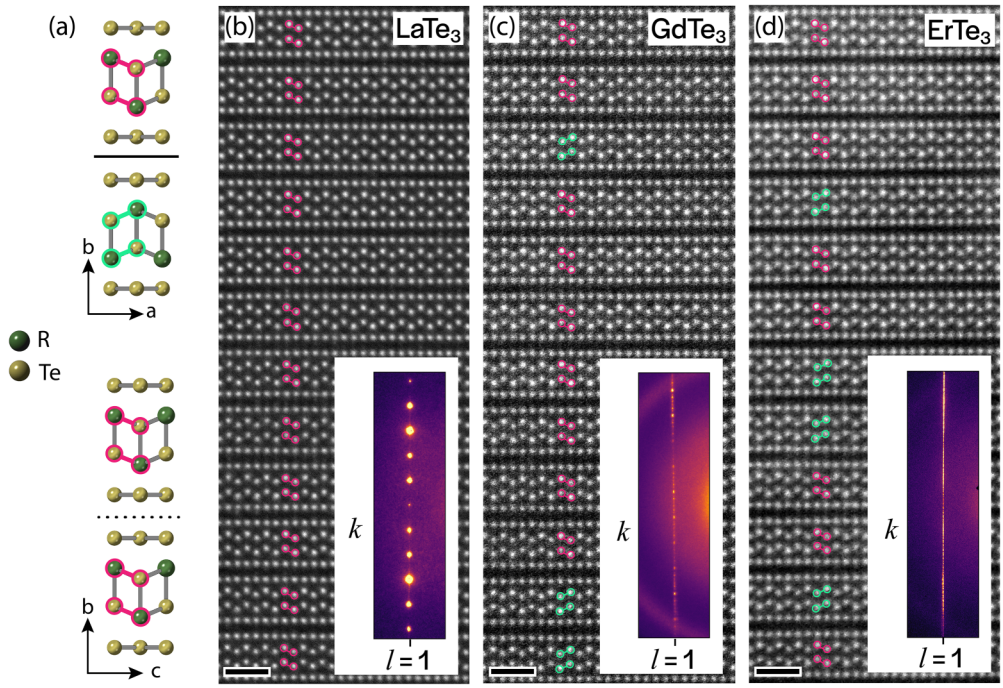

FIG. 1. Stacking defects in $R\text{Te}_3$. (a) Schematic of $R\text{Te}_3$ crystal structure as viewed in the **c** axis (top panel) and **a** axis (bottom panel). Notice the **c** glide in the *bc* plane projection, i.e., [100] zone axis [dotted line in (a), bottom schematic]. Solid line in the top schematic in (a) represents mirror plane. Cross-section HAADF-STEM images of exfoliated (b) LaTe_3 (c) GdTe_3, and (d) ErTe_3. The insets in (b–d) show electron diffraction from (0 k 1) planes; smearing of the spots implies disordered stacking (Supplemental Fig. S2 [26] shows the regions of the samples from which the SAED patterns were taken as well as the full SAED patterns). Scale bars are 1 nm.

[22] studied this lattice-CDW coupling by applying in-plane strain to bulk ErTe_3 crystal. Unstrained ErTe_3 undergoes two successive CDW phase transitions, with $T_{\text{CDW1}} \approx 260$ K and $T_{\text{CDW2}} \approx 160$ K. When ErTe_3 is strained to make $|\boldsymbol{a}| = |\boldsymbol{c}|$, the two critical temperatures become equal and the system directly enters the bidirectional CDW state [22]. The CDWs can also be affected by defects. For example, when point defects were introduced by intercalating Pd in ErTe_3, a pronounced effect on the CDWs was observed, and at high defect concentrations, CDWs were suppressed and a Bragg glass phase was observed [23–25].

While prior studies demonstrate the effects of strain and point defects on the CDWs in $R\text{Te}_3$, a spatially resolved microscopic study is needed to directly link the CDW orders to local microstructure. We image the local microstructures of exfoliated flakes of $R\text{Te}_3$ (R = La, Gd, and Er) and probe their effects on the CDW phases, while also performing *ab initio* density-functional theory (DFT) calculations of stacking fault energies, of preferred planar sliding directions, and of the impact of stacking faults on the crystal symmetry. In perfect harmony with our *ab initio* findings, atomic-resolution STEM imaging reveals basal dislocations in $R\text{Te}_3$ that change the layer stacking order, reducing the in-plane anisotropy in the crystal, making it pseudotetragonal. Using electron diffraction and four-dimensional STEM (4D STEM) at cryogenic temperature, we correlate the microstructural features of $R\text{Te}_3$ flakes with their CDW behavior and find that in the presence of dislocations: (1) the high-temperature CDW_1 is stabilized along both in-plane axes instead of only along the **c** axis and (2) the low-temperature CDW_2 is suppressed in the bidirectional CDW system. We also show dislocations in the CDW lattice, which appear uncorrelated with the crystal defects. We observe that $R\text{Te}_3$'s with smaller rare-earth elements are more susceptible to developing stacking defects. This work provides microscopic information on the defect-CDW interaction, which is essential in understanding the static and dynamic properties of CDW states and provides a possibility to engineer CDWs for device applications.

II. RESULTS AND DISCUSSION

A. Stacking defects in $R\text{Te}_3$

Figure 1(a) shows the $R\text{Te}_3$ crystal structure in the [001] and [100] zone axes (*ab* and *bc* planes, respectively). The unit cell consists of two $R\text{Te}_3$ layers where the layers are symmetric under a translation by $\boldsymbol{c}/2$ followed by reflection across the plane perpendicular to the **b** axis. Thus a glide plane perpendicular to the **b** axis exists, with the glide direction only along the **c** axis and not the **a** axis (**c** glide). To observe this anisotropic glide symmetry, cross-section samples of exfoliated flakes were prepared using a focused ion beam and imaged using an aberration-corrected scanning transmission electron microscope and a high-angle annular dark field (HAADF) detector (details in Supplemental Note 1 in the Supplemental Material [26]; also see Refs. [27–38]). These cross-sectional HAADF-STEM images of LaTe_3, GdTe_3, and ErTe_3 flakes show the layer stacking in the samples [Figs. 1(b)–1(d)]. Surprisingly, we observe stacking defects in GdTe_3 and ErTe_3, where the stacking changes are highlighted in pink and green. For LaTe_3 and GdTe_3 with no or just a few stacking defects [Figs. 1(b) and 1(c)], our measurements clearly show the expected projection along the [100] zone axis

(**a** axis). For $GdTe_3$, the local unit cell at the defect plane resembles the [001] projection of the unit cell while the remainder of the sample retains the [100] projection. In the case of $ErTe_3$, many stacking defects are present [Fig. 1(d)]; thus it is not clear if the sample was imaged in the [100] or [001] zone axis. Therefore, in the presence of stacking defects, the anisotropic presence of the **c** glide is lost and the two in-plane axes cannot be unambiguously determined. Cross-sectional HAADF-STEM images from the same flakes but viewed in the [001] zone axis (**c** axis) are shown in Supplemental Fig. S1 [26], where the stacking defects again increase when going from $LaTe_3$ to $ErTe_3$.

Since HAADF-STEM images represent a small field of view, selected area electron diffraction (SAED) patterns were acquired from several micron-wide regions, as shown in the insets of Figs. 1(b)–1(d) and Supplemental Figs. S1(a)–S1(c) [26] (Supplemental Fig. S2 shows the cross-section regions from which the SAED patterns were taken). Since stacking changes disrupt the interlayer periodicity, the stacking defects in RTe_3 result in the smearing of the $(0\,k\,l)$ and $(h\,k\,0)$ diffraction spots in the [100] and [001] zone axes, respectively. Here h and l are odd integers. The stacking disorder increases with smaller rare-earth elements as evidenced by more pronounced smearing of the diffraction peaks going from $LaTe_3$ to $ErTe_3$. While far rarer than in $GdTe_3$ and $ErTe_3$, we note that stacking defects are still observed in $LaTe_3$ flakes.

B. DFT calculations of stacking defects

To corroborate the observed stacking faults in RTe_3 and to estimate the likelihood of generating such defects, DFT calculations were carried out on a $LaTe_3$ supercell (see Supplemental Note 1 [26]). We constructed two periodic supercells containing four $LaTe_3$ layers, one without a stacking fault (A, B, A, B) and one with a stacking fault (A, B, A, B′), as shown in Fig. 2(a). Here B denotes a shift of (a/2, 0, 0) from the A layer so that the Te square nets between adjacent $LaTe_3$ layers do not lie atop each other. The bulk stacking in RTe_3 corresponds to (A, B) stacking [Fig. 2(a)]. B′ indicates an in-plane rotation of 90 ° to the B layer or alternatively a shift of (0, 0, a/2) from the A layer. This corresponds to a stacking fault density of 0.25 per $LaTe_3$ formula unit.

In the absence of stacking faults, after structural relaxation, we find $a = 4.395\,54$ Å, $c = 4.395\,93$ Å, and $b = 13.3194$ Å, indicating a very slight breaking of the square lattice symmetry as expected. While this ∼0.0085% (∼0.04 pm) difference between a and c is smaller than the reported values [21], it is persistent and roughly constant across a wide range of wave-function plane-wave energy cutoffs of 15–40 hartrees (electron-density cutoffs of 75–280 hartrees). With the inclusion of a stacking fault, however, the square lattice symmetry is retained within our convergence tolerance with $a = 4.395\,75$ Å, $c = 4.395\,77$ Å, and $b = 13.3193$ Å. In other words, the inclusion of a stacking fault converts $LaTe_3$ from a weakly orthorhombic lattice to a tetragonal lattice. We note that the calculated change in the lattice parameters $|\boldsymbol{a}|$ and $|\boldsymbol{c}|$ due to stacking faults could not be confirmed experimentally using atomic imaging or electron diffraction due to experimental limitations.

To estimate the energy cost per unit area of including a stacking fault, we compute the energy difference between the above two calculations, which represents the stacking fault energy. While the stacking faulty energy is at the resolution limit of our calculation and, as such, does not smoothly converge with respect to plane-wave cutoff, we do find the stacking fault energy to be consistently positive, with a value we estimate to lie somewhere around, and no more than, $0.035-0.117\,\mathrm{mJ/m^2}$.

To create a stacking fault, interlayer sliding between two neighboring $LaTe_3$ layers is necessary, so that defect formation depends on the energy landscape as layers slide relative to each other. Figure 2(b) shows the stacking energy relative to the ground-state "bulk" configuration as a function of relative displacement for 20 stacking configurations along the high-symmetry directions, revealing the kinetic barrier that must be crossed to generate the defect via interlayer sliding. As expected, bulk stacking, where the Te square net of one $LaTe_3$ layer sits atop the holes of the Te square net of another layer [labeled "Te/Center" in Fig. 2(b)], has the lowest stacking energy. We also find that direct stacking of the Te square nets ["Te/Te" in Fig. 2(b)] is the least favorable (stacking energy of $89.5\,\mathrm{mJ/m^2}$ relative to bulk), so that sliding in the [100] or [001] directions is energetically unfavorable. In contrast, sliding in the [101] direction has the smallest energy barrier ($53.8\,\mathrm{mJ/m^2}$), so that we expect stacking defects with interlayer sliding components in the [101] direction to be the most likely to form. We note that the energies associated with interlayer sliding are two orders of magnitude larger than our computed stacking fault energy and are well resolvable with our pseudopotentials.

C. Dislocations and stacking defects

Interlayer sliding required to create stacking defects can occur in the presence of dislocations. Figure 2(c) shows a cross-section image of $LaTe_3$ in the [001] zone axis, which shows a dislocation with a projected Burgers vector $\boldsymbol{B}_{\mathrm{proj}} = \frac{1}{2}[100]$. A Burgers circuit is drawn with white dotted lines, enclosing the dislocation core. The observed dislocation core cannot be in the R-Te corrugated block since that would exhibit a Burgers component along the **b** axis, which we do not observe. Further, a dislocation core in the R-Te block is energetically unfavorable as the R and Te sites need to exchange their positions, creating rows of antisite defects. Thus, we believe the dislocation core lies in the Te square net. Based on the DFT calculations that suggest that interlayer sliding along [101] is most energetically favorable, we infer that the true Burgers vector $\boldsymbol{B}$ must be $\frac{1}{2}[101]$.

In Fig. 2(c), the layer stacking to the left of the dislocation core resembles that of the [100] projection [see Fig. 1(a)], but to the right of the core, it resembles the [001] projection. Thus the **a** and **c** axes are effectively swapped across the dislocation, changing the layer stacking locally. Figure 2(d) shows the simulated HAADF-STEM image of $LaTe_3$ in cross section, having our proposed dislocation structure with $\boldsymbol{B} = \frac{1}{2}[101]$, which captures the experimentally observed smearing of atoms around the dislocation core and the stacking change from the [100] projection to the [001] projection across the dislocation core in full agreement with the experiment.

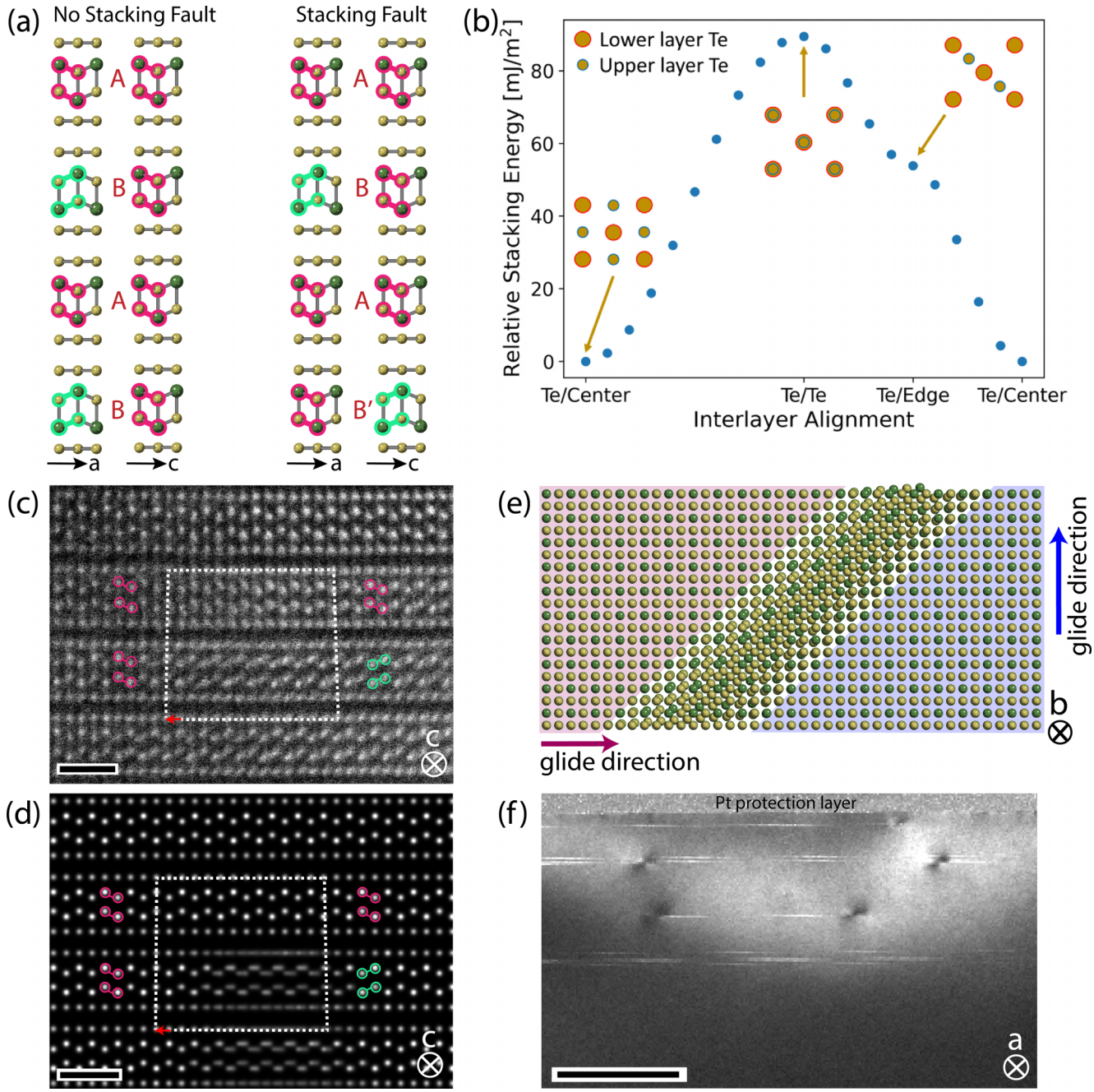

FIG. 2. Relation between stacking defects and dislocation in RTe$_3$. (a) LaTe$_3$ supercells used for DFT calculations. (b) Interlayer stacking energy of a LaTe$_3$ bilayer relative to the bulk stacking energy. The horizontal axis denotes the high-symmetry path between high-symmetry stacking, with the labels denoting the relative positions of the adjacent Te square nets relative to the two LaTe$_3$ layers. The inlays show the Te square nets of the three stacking arrangements. Shifting in the [101] direction by (a/2, 0, a/2) from Te/center to Te/edge and then back to Te/center has the smallest energy barrier due to Te/edge being a saddle point in the interlayer stacking energy. (c) Cross-sectional view of LaTe$_3$ showing a dislocation (a Burgers circuit is shown by the white dotted line, and the component of the Burgers vector in the viewing direction is shown by the red arrow). The layer stacking changes across the dislocation core. Scale bar = 1 nm (d) Multislice HAADF-STEM simulation of LaTe$_3$ in cross section containing a $\frac{1}{2}$[101] dislocation, which matches the experimental HAADF-STEM image in (c). (e) Schematic of the same dislocation in (d), viewed in the [010] projection. Across the dislocation, the in-plane **a** and **c** axes swap and hence the glide direction realigns. (f) Virtual DF-STEM image of GdTe$_3$ reconstructed for the forbidden (031) reflections in the [100] zone axis. The white streaks correspond to the stacking changes where the local zone axis is [001] and (130) reflections [counterpart to (031) reflections in the [001] zone axis] are allowed. Scale bar = 0.5 μm.

The presence of a dislocation with $\boldsymbol{B} = \frac{1}{2}[101]$ therefore results in a stacking change. The swapping of **a** and **c** axes locally can also be thought of as realignment of the glide direction from the **c** axis to the **a** axis. This is schematically illustrated in Fig. 2(e) viewed along the **b** axis (normal to basal planes).

The swapping of local **a** and **c** axes due to dislocations is imaged over a larger field of view using 4D STEM. In 4D STEM, a nanoscale electron beam is rastered across the sample and 2D diffraction patterns are collected at each probe position [39]. Figure 2(f) shows a virtual dark-field (DF) STEM image of a cross-section sample of bulk $GdTe_3$ crystal in the [100] zone axis, reconstructed from the forbidden (031) Bragg reflection. Since its counterpart (130) is allowed in [001], wherever the stacking matches that of [001] projection, the region appears brighter in the virtual DF image. In other words, the white streaks in the image correspond to stacking defects, where the in-plane axes have flipped. Additionally, we see that these stacking defects are bound by features that have darker contrast. The contrast change is a result of local deviation from the regular crystal lattice and is typical of dislocations [40]. This again shows that dislocations change the stacking order in $R\mathrm{Te}_3$.

In summary, the DFT calculations show that an inclusion of a stacking fault leads to a square net of Te, converting the crystal from a weak orthorhombic lattice to a tetragonal lattice, and the estimated energy for stacking defects is small with the preferred sliding direction of [101]. This agrees with the experiment where a dislocation with $\boldsymbol{B} = \frac{1}{2}[101]$ locally swaps the two in-plane axes, which leads to the loss of the anisotropic presence of the **c** glide and orthorhombicity. If the dislocation density is low, then the crystal would retain its orthorhombic nature overall, and we would expect previously observed bulk behaviors with CDW_1 aligned along the **c** axis. In contrast, if the dislocation density is high, the exfoliated crystals will eventually become pseudotetragonal at high enough dislocation densities and a change in the CDW behavior is expected.

D. Effects of pseudotetragonality on the CDW

To study the effects of dislocation on the CDW behavior, we imaged exfoliated flakes of $LaTe_3$, $GdTe_3$, and $ErTe_3$ at 100 K using bright-field TEM (BF TEM) and SAED in the [010] zone axis (plan view). An extensive network of basal dislocations is observed in these exfoliated flakes, which appear as dark lines in BF-TEM images [Figs. 3(b), 3(c), and 3(f)], similar to what is observed in other layered materials [40]. Figure 3(a) shows schematics of the expected SAED patterns for pristine $R\mathrm{Te}_3$ with no CDW, unidirectional CDW, and bidirectional CDW in the absence of any defects. The circles represent the Bragg peaks from the lattice, and the upright and upside-down triangles represent the satellite peaks from CDW_1 and CDW_2, respectively. In regions of the $LaTe_3$ and $GdTe_3$ flakes that contain few defects, the SAED patterns show the expected CDW behavior with the CDW_1 satellite peaks appearing only along one of the in-plane axes [Figs. 3(b) and 3(c), area 1], presumably along the $\boldsymbol{c}^*$ direction (asterisk (*) here denotes a reciprocal lattice vector). In contrast and surprisingly, the regions of the $LaTe_3$ and $GdTe_3$ flakes that contain many dislocation lines show SAED patterns with CDW satellite peaks present along both the $\boldsymbol{a}^*$ and $\boldsymbol{c}^*$ directions [Figs. 3(b) and 3(c), area 2]. This behavior has not been observed in $LaTe_3$ and $GdTe_3$ bulk crystals, which are unidirectional CDW systems. Similar observations were reported for $TbTe_3$ using STM, but the finding was attributed to surface effects [41]. We observe CDW_1 peaks along both the $\boldsymbol{a}^*$ and $\boldsymbol{c}^*$ axes up to room temperature (Supplemental Fig. S3 [26]). Thus we show that pseudotetragonality due to dislocations lifts the directional preference of CDW_1.

The low-temperature CDW_2 is also impacted by the presence of dislocations and the resulting loss of orthorhombicity. This is probed in an exfoliated $ErTe_3$ flake, which should exhibit a bidirectional CDW state (coexisting CDW_1 along $\boldsymbol{c}^*$ and CDW_2 along $\boldsymbol{a}^*$) below ~160 K. From bulk studies, the magnitudes of the CDW wave vectors for $ErTe_3$ are $\boldsymbol{q}_{CDW1} = 0.300\boldsymbol{c}^*$ and $\boldsymbol{q}_{CDW2} = 0.313\boldsymbol{a}^*$ [21]. The SAED pattern at 100 K from a defect-free region shows this expected behavior with different magnitudes for the two wave vectors [$|\boldsymbol{q}_2| > |\boldsymbol{q}_1|$, Figs. 3(d) and 3(e)], but from a region that has a high defect density, the SAED pattern shows that the two wave vectors have comparable magnitudes [$|\boldsymbol{q}_2| \approx |\boldsymbol{q}_1|$, Figs. 3(f) and 3(g)]. Figures 3(h) and 3(i) show the magnitude of the two orthogonal $\boldsymbol{q}$ vectors as a function of temperature. For an $ErTe_3$ flake that is defect free, the two $\boldsymbol{q}$ vectors start to have different magnitudes at temperatures <200 K, indicating the low-temperature CDW_2 emerges below 200 K [Fig. 3(h)]. Surprisingly, for the highly defective flake, the two $\boldsymbol{q}$ vectors remain $\sim 0.300\boldsymbol{a}_i^*$ ($i = 1$ or 2) at all temperatures [Fig. 3(i)]. This implies that, when the local orthorhombicity is lost due to defects, CDW_1 is populated along both in-plane axes, and the lower-temperature CDW_2 is suppressed. This behavior also suggests that the two CDW orders compete with each other, in agreement with the recent pump-probe study [42]. Supplemental Fig. S4 [26] shows the variation of the two $\boldsymbol{q}$ -vectors for another defect-free $ErTe_3$ flake from 16 to 240 K.

E. Correlation of CDW domains with defects by 4D STEM

From the SAED patterns, we establish that the presence of dislocations leads to the emergence of CDW_1 along both in-plane axes and suppression of CDW_2. Because SAED averages over micron-wide regions, it is unclear if the two CDW_1 orders, aligned orthogonally along both axes, spatially coexist or are separated into domains. To characterize the spatial distribution of the CDW order at the nanoscale, we acquired 4D-STEM data from $ErTe_3$ at temperatures ranging from 120 to 300 K.

Figure 4(a) shows a reconstructed DF-STEM image of an $ErTe_3$ flake (see Supplemental Note 2 [26] for details on the 4D-STEM analysis). Similar to the flakes in Fig. 3, the straight lines observed in the flake indicate dislocations. Note that $ErTe_3$ at 120 K should be in a bidirectional state with coexisting CDW_1 and CDW_2. Diffraction data from two probe positions [Fig. 4(a)] show that at the probe position P_1, the CDW satellite peaks are stronger along $\boldsymbol{a}^*$, while at probe position P_2, the peaks are stronger along $\boldsymbol{c}^*$ (The **a** vs **c** axes are inferred from the analysis shown in Figs. 4(f) and 4(g). Hence, the CDW order is not spatially uniform in the flake and may be correlated with the flake's microstructure.

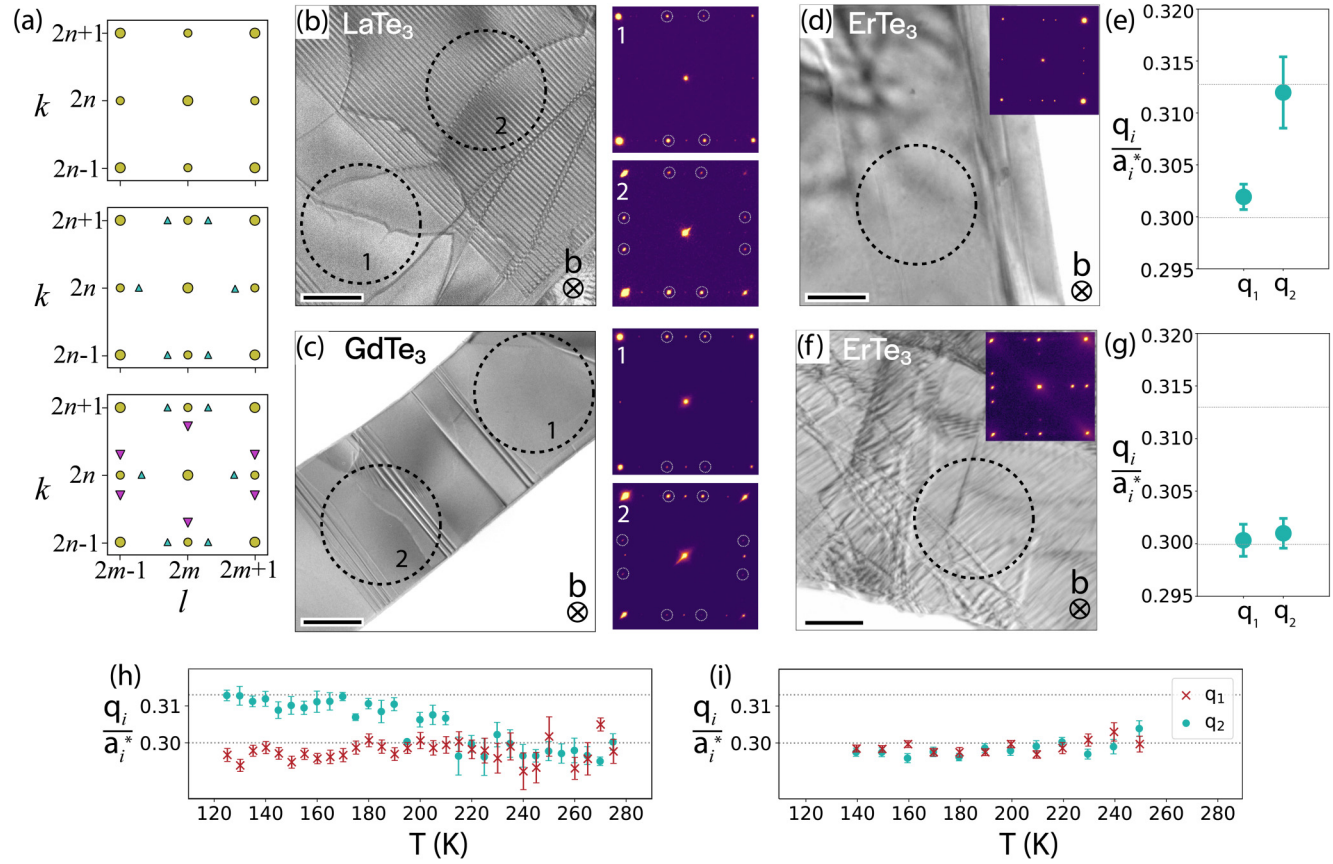

FIG. 3. Effects of defects on the CDW behavior. (a) Schematic diffraction patterns in the [010] zone axis when $R\text{Te}_3$ are in the high-temperature phase (no CDW) showing only Bragg peaks (circles). In the unidirectional CDW state satellite peaks emerge along one of the crystallographic directions (upright triangles). In the bidirectional CDW state, another set of satellite peaks emerges (upside-down triangles) and these peaks are orthogonal to the first CDW. Plan-view BF-TEM images of exfoliated flakes of (b) $LaTe_3$ and (c) $GdTe_3$ showing diffraction contrast from dislocations and stacking defects. Corresponding SAED patterns collected from encircled regions are shown adjacent to the BF-TEM images. The satellite peaks are encircled. (d) $ErTe_3$ flake with low defect density. Inset shows the diffraction pattern. (e) Measuring the two CDW wave vectors gives the expected bulk values. (f) $ErTe_3$ with higher defect density, and (g) shows that the two wave vectors are equal in magnitude. (h,i) Temperature evolution of the wave vectors in two $ErTe_3$ flakes. (h) is characterized by a low defect density, while (i) is from a flake with a high defect density. Horizontal dotted lines in (e,g–i) correspond to the bulk $\boldsymbol{q}$-vector magnitudes. Since we do not know the crystal axes, we use the notations $\boldsymbol{a}_1$ and $\boldsymbol{a}_2$ for the lattice vectors, and $\boldsymbol{q}_1$ and $\boldsymbol{q}_2$ for the CDW wave vectors in two orthogonal directions. Scale bars are 0.25 μm.

CDW mapping images are generated by applying virtual apertures to the CDW peaks along $\boldsymbol{a}^*$ or $\boldsymbol{c}^*$ in the 4D-STEM data at each probe position [43] (see Supplemental Note 2 and Supplemental Fig. S5 for the analysis details [26]). Figures 4(b) and 4(c) show these images at 120 K. Intensity in these CDW mapping images represents the CDW peak intensity and, hence, the spatial distribution of the CDW along $\boldsymbol{a}$ or $\boldsymbol{c}$ (Note: $\boldsymbol{a} \parallel \boldsymbol{a}^*$; $\boldsymbol{c} \parallel \boldsymbol{c}^*$). From Fig. 4(b), CDW along $\mathbf{a}$ is found in most of the flake, although in the rectangular region separated by the defects (marked by dotted lines), this CDW order is weak, indicating two different domains. As an alternative method to visualize the CDW domains, we also count the number of CDW peaks along $\boldsymbol{a}^*$ at each probe position. This reveals fewer satellite peaks along $\boldsymbol{a}^*$ in the small rectangular domain [Fig. 4(d)], in agreement with weaker CDW in this domain [Fig. 4(b)] (see Supplemental Note 2 [26] for details in CDW peak counting). From Figs. 4(c) and 4(e), CDW aligned along $\boldsymbol{c}$ is more uniformly distributed, with slightly higher intensity in the rectangular region where CDW along $\boldsymbol{a}$ is weaker. Thus, although the CDWs along both $\boldsymbol{a}^*$ and $\boldsymbol{c}^*$ are present in the flake, CDW peaks along $\boldsymbol{a}^*$ are stronger in the larger domain, while the CDW peaks along $\boldsymbol{c}^*$ are much stronger than the peaks along $\boldsymbol{a}^*$ in the rectangular domain.

Bulk $ErTe_3$ shows a bidirectional CDW with wave vectors $\boldsymbol{q}_{\text{CDW1}} = 0.300\boldsymbol{c}^*$ and $\boldsymbol{q}_{\text{CDW2}} = 0.313\boldsymbol{a}^*$ at 120 K [21]. To distinguish whether the observed CDWs are bidirectional similar to bulk, or unidirectional CDW_1 along both in-plane axes, we measure the CDW wave-vector magnitude for $\boldsymbol{q}_1(\parallel \boldsymbol{a}^*)$ and $\boldsymbol{q}_1(\parallel \boldsymbol{c}^*)$ from the 4D-STEM data, which are shown in Figs. 4(f) and 4(g). In the rectangular domain (marked by dotted lines), we obtain average wave-vector magnitudes of $0.306\,99(33)|\boldsymbol{a}^*|$ and $0.291\,76(23)|\boldsymbol{c}^*|$. While both wave vectors are less than the expected bulk values, the magnitude of $\boldsymbol{q}_1$ is greater than $\boldsymbol{q}_2$, indicating that the defect density is lower in this region and the sample retains its orthorhombicity, at least locally. In the rest of the flake, we obtain $0.299\,15(5)|\boldsymbol{a}^*|$ and $0.293\,20(9)|\boldsymbol{c}^*|$, which indicates that this CDW is the high-temperature unidirectional CDW_1, populated along both

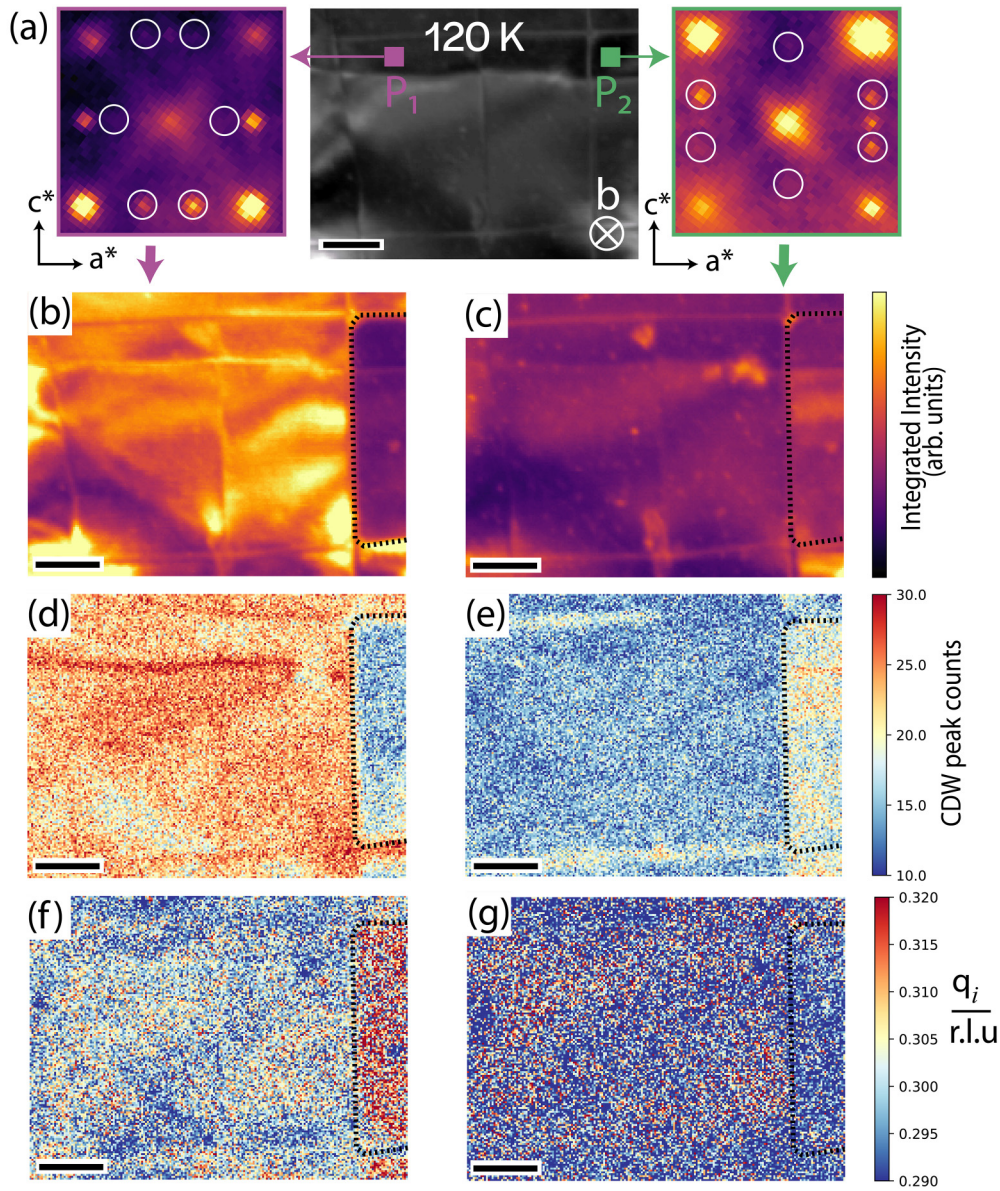

FIG. 4. Real-space distribution of CDWs in $ErTe_3$. (a) Reconstructed real-space image from 4D STEM showing an $ErTe_3$ flake at 120 K. Diffraction patterns from two pixel locations are shown; notice the CDW order is different. Overlaid on these diffraction patterns are virtual apertures (white circles) selecting CDW reflections only along one of the reciprocal lattice vectors. (b,c) CDW intensity maps reconstructed from the two virtual apertures in (a). The dashed lines separate two domains with different CDW behavior. (d,e) CDW peak count maps, plotting the number of CDW peaks detected along $\boldsymbol{a}^*$ and $\boldsymbol{c}^*$. (f,g) Maps plotting the magnitude of the CDW wave vectors at 120 K (r.l.u. = reciprocal lattice units). Scale bars are 0.25 μm.

in-plane axes. Thus most of the flake is pseudotetragonal, which can occur in the presence of dislocations that locally realign the glide direction (Fig. 2).

Supplemental Videos S1 and S2 [26] show the CDW mapping images as temperature is varied between 120 and 300 K. CDW_2 in the small rectangular domain melts away when $T > 200$ K. CDW_1 peaks disappear at ∼260 K, similar to the bulk behavior. Supplemental Videos S3 and S4 [26] show the CDW wave-vector maps of the $ErTe_3$ flake as a function of temperature from 120 to 200 K, again showing the melting of CDW_2 in the bidirectional domain. The overall intensity of the CDW maps (in Supplemental Videos S1 and S2 [26]) gradually increases due to the increased thermal diffuse scattering in diffraction patterns at higher temperatures. Supplemental Video S5 [26] shows this effect prominently with increasing background intensity of the Kikuchi bands in averaged diffraction patterns from the pseudotetragonal domain of the flake in Fig. 4(a) at different temperatures.

We also performed *in situ* cryo-4D-STEM on exfoliated flakes of $LaTe_3$ and observed similar spatially separated domains: an orthorhombic domain that contains a unidirectional CDW (bulk behavior) and a pseudotetragonal domain that contains CDWs along two in-plane directions (Supplemental Fig. S6 [26]). Unsupervised machine learning was employed as an alternative, less time-consuming analysis, requiring minimal user input, to extract the microstructural details of the

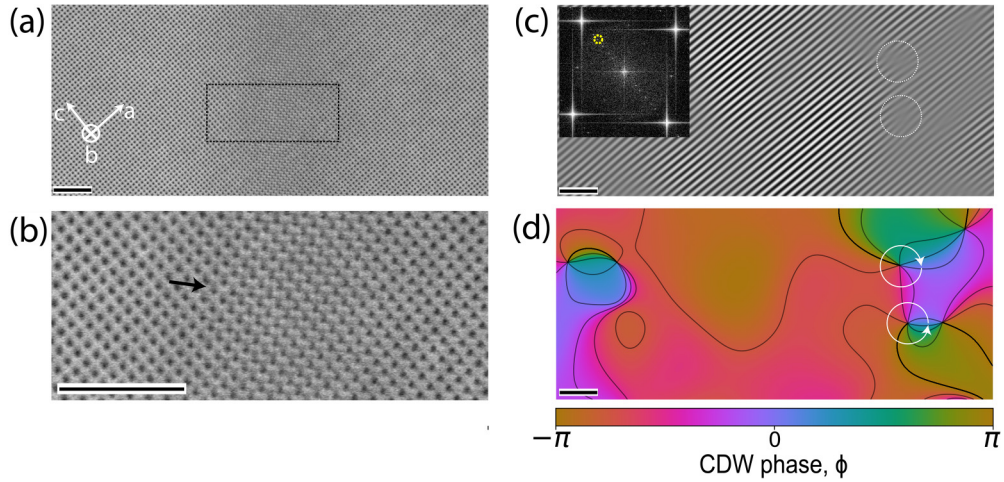

FIG. 5. Dislocations in the CDW of $LaTe_3$. (a) Atomic-resolution BF-STEM image of $LaTe_3$, with a dislocation (also see Supplemental Fig. S8 [26]). (b) An enlarged view of the image in (a); the smearing of atoms due to dislocation is similar to Fig. 2(e). (c) Fourier-filtered image showing the local periodicity of the CDW (plot of the real part of the inverse FFT). CDW dislocations are encircled. The CDW peak used to filter is shown in the inset and Supplemental Fig. S7 [26]. (d) Extracted phase from the Fourier-filtered image. At the CDW dislocations, the phase winds by 2π. The arrows show the phase winding is reversed for each dislocation in a pair. The contours on the image show a phase change of $\pi/4$. Scale bars are 2 nm.

CDW by clustering 4D-STEM datasets (Supplemental Note 3 [26]).

F. Discussion

Our analysis of SAED patterns showed that CDW_1 is present along both in-plane directions in regions with high defect density, and from 4D STEM we found that these two CDW_1's coexist in real space when averaging through the thickness of the sample along the **b** axis. An outstanding question remains: whether the two CDW_1 orders spatially overlap and coexist within the same Te square net or if each Te net hosts a single CDW_1 order along the local glide direction. While this is challenging to determine using (S)TEM due to the thickness-averaged information it provides, we hypothesize that the two CDW_1 orders coexist within the same Te net. Previous STM measurements on $TbTe_3$ support this hypothesis by demonstrating that the surface Te net can host the two unidirectional CDW states [41]. Moreover, if each Te net can host only one CDW_1 order parallel to the local **c** axis, CDW_2 does not need to be suppressed as CDW_1 is aligned along only one axis, locally. Thus thickness-averaged diffraction of $ErTe_3$ will have both CDW_1 and CDW_2 peaks along two in-plane axes. Since the magnitudes of $\boldsymbol{q}_{CDW1}$ and $\boldsymbol{q}_{CDW2}$ are different, we would expect to see two distinct peaks along both $\boldsymbol{a}^*$ and $\boldsymbol{c}^*$. However, experimental observations contradict this anticipated outcome.

We now address the possible origin of the dislocations that change the stacking. The most likely origin is mechanical exfoliation, which introduces shear stresses in the flakes during exfoliation. It is inferred from the virtual dark-field (DF) image of our bulk $GdTe_3$ crystal [Fig. 2(f)], where the stacking defects (appearing as white streaks) are concentrated near the surface of the crystal and gradually disappear going into the crystal away from the top surface. Given that exfoliation-related stresses would be the highest at the surface where flakes separate from the bulk crystal, the observed defect distribution supports our hypothesis of exfoliation-induced stacking faults. The very low stacking fault energies found in our DFT studies further support this conclusion. We note, however, that intrinsic materials properties may also be at play as we recently observed in other 2D materials [44]. Relevant in this case may be the size of the rare-earth element in RTe_3, which influences the formation of dislocations and, consequently, stacking defects as we observe an increasing stacking defect density from $LaTe_3$ to $ErTe_3$.

G. Dislocations in the CDW

A CDW is an electronic crystal and, like any other crystal, can exhibit dislocations [45]. To visualize CDW dislocations in real space, we imaged $LaTe_3$ in the [010] zone axis using atomic-resolution bright-field (BF) STEM [Fig. 5(a)]. A fast-Fourier transform (FFT) of this image shows its reciprocal space structure, reflecting both the lattice periodicity and CDW modulation. As the Te atoms in the square net are in the same atomic column as the La atoms in this zone axis, atomic displacements in the Te atoms from the CDW are not discernible in the image. To visualize the CDW modulation in real space, we create a Fourier-filtered image by masking everything except the CDW peaks at $\boldsymbol{q}_{CDW1,LaTe3} = \pm 0.288\boldsymbol{c}^*$ in the FFT (inset of Fig. 5(c) and Supplemental Fig. S7 [26]) and then performing an inverse FFT [Fig. 5(c)]. In the Fourier-filtered image, we observe discontinuities in the CDW periodicity, which have the appearance of extra half planes [encircled in Fig. 5(c)]. Next we extract the geometric phase information from the Fourier-filtered image as described in Ref. [46], which shows the CDW phase winds by 2π around the discontinuities [Fig. 5(d)]. Hence, these discontinuities are identified as dislocations in the CDW lattice [4]. We note that we always find dislocations-antidislocation pairs (two dislocations that have opposite phase winding) in the CDW

lattice (Figs. 5(c) and 5(d) and Supplemental Fig. S8 [26]). We note that that these CDW dislocations are not related to the structural dislocations which were discussed under Dislocations and stacking defects (Sec. II C).

Figure 5(a) also shows a structural dislocation running vertically in the center of the BF-STEM image of $LaTe_3$ (Fig. 5(b) and Supplemental Fig. S8 [26] shows a larger field of view). Because of atomic displacements, the dislocation line appears as smearing of atomic columns [Fig. 5(b)]. BF-STEM images were simulated using different dislocation models to replicate Fig. 5(b) and are shown in Supplemental Fig. S9 [26]. Comparing the positions of the structural dislocation [Fig. 5(a)] to the CDW dislocations [Figs. 5(c) and 5(d)], the CDW dislocation pairs appear spatially independent from the visible structural dislocation. This is surprising because a correlation between CDW dislocation and structural dislocations was anticipated based on the previously reported response of $R\mathrm{Te}_3$ to disorder potentials [23,24]. The disorder is highest in the vicinity of a structural dislocation core. Thus, while the presence of structural dislocations controls the layer stacking order and orthorhombicity, which influences the nature of CDW, the direct, real-space interaction of structural dislocations with CDW dislocations appears minimal.

III. CONCLUSION

In conclusion, we employed *in situ* cryo-STEM and 4D STEM to study microscopically the effects of structural defects on the CDW phases of $R\mathrm{Te}_3$'s. We find that dislocations are present in exfoliated flakes, likely created during the mechanical exfoliation, with the basal dislocations creating stacking defects that swap the direction of the glide planes. This finding is also supported by *ab initio* DFT calculations revealing extremely low stacking fault energies, showing a preference for sliding along the [101] direction. When the stacking fault density is high, both experiments and theory show the orthorhombicity is lost and the crystal becomes pseudotetragonal, which ultimately leads to the population of the high-temperature, unidirectional CDW along both in-plane directions and the suppression of the low-temperature CDW (in systems with bidirectional CDW). We observe that dislocations spatially separate the pseudotetragonal domains from the orthorhombic domains, where the latter shows CDW characteristics close to bulk behavior owing to a lower defect density. Finally, we visualize dislocations in the CDW at the atomic scale, finding dislocation-antidislocation pairs. The presence of these dislocation pairs will influence the electronic properties of $R\mathrm{Te}_3$'s, by affecting the phase coherence of the CDWs, changing the dynamics of CDW sliding [47,48], and stabilizing competing orders like superconductivity at the dislocation cores [49]. This work highlights the importance of atomic-scale defects and their influence on systems with macroscopic quantum states.

ACKNOWLEDGMENTS

In situ cryo-4D-STEM experiments were supported by the Department of Energy, Basic Energy Sciences program Grant No. DE-SC0023905. This work made use of facilities and instrumentation supported by NSF through the Cornell University Materials Research Science and Engineering Center Award No. DMR-1719875, and the Platform for the Accelerated Realization, Analysis, and Discovery of Interface Materials (PARADIM) Award No. DMR-2039380. PARADIM (Award No. DMR-2039380) also provided full time support for D.N. and partial support for T.A.A. The FEI Titan Themis 300 was acquired through Grant No. NSF-MRI-1429155, with additional support from Cornell University, the Weill Institute, and the Kavli Institute at Cornell. This work was performed in part at the Cornell NanoScale Facility, an NNCI member supported by NSF Grant No. NNCI-2025233. The work at Brookhaven National Laboratory was supported by U.S. DOE-BES, Materials Sciences and Engineering Division under Contract No. DE-SC0012704. The work at Princeton was supported by the Gordon and Betty Moore Foundation's EPIQS initiative through Grant No. GBMF9064, the David and Lucille Packard foundation, and by the Air Force Office of Scientific Research under Award No. FA9550-20-1-0246. N.S. acknowledges additional support from the NSF GRFP under Award No. DGE- 2139899.

[1] A. H. Cottrell, Theory of dislocations, Prog. Metal Phys. **1**, 77 (1949).
[2] N. F. Mott, Dislocations and the theory of solids, Nature (London) **171**, 4345 (1953).
[3] W. W. Webb, Dislocations in superconductors, Phys. Rev. Lett. **11**, 191 (1963).
[4] D. F. Agterberg and H. Tsunetsugu, Dislocations and vortices in pair-density-wave superconductors, Nat. Phys. **4**, 8 (2008).
[5] H. H. Weitering, J. M. Carpinelli, A. V. Melechko, J. Zhang, M. Bartkowiak, and E. W. Plummer, Defect-mediated condensation of a charge density wave, Science **285**, 2107 (1999).
[6] T.-H. Kim and H. W. Yeom, Topological solitons versus nonsolitonic phase defects in a quasi-one-dimensional charge-density wave, Phys. Rev. Lett. **109**, 246802 (2012).
[7] L. Nie, G. Tarjus, and S. A. Kivelson, Quenched disorder and vestigial nematicity in the pseudogap regime of the cuprates, Proc. Natl. Acad. Sci. USA **111**, 7980 (2014).
[8] D. Feinberg and J. Friedel, Elastic and plastic deformations of charge density waves, J. Phys. (Paris) **49**, 485 (1988).
[9] S. N. Artemenko, F. Gleisberg, and W. Wonneberger, Mobility of gliding dislocation loops and their contribution to the conductivity of CDW-conductors, J. Phys. IV **09**, Pr10 (1999).
[10] J. L. Hart, S. Siddique, N. Schnitzer, S. D. Funni, L. F. Kourkoutis, and J. J. Cha, In operando cryo-STEM of pulse-induced charge density wave switching in TaS_2, Nat Commun **14**, 1 (2023).
[11] H.-M. Eiter, M. Lavagnini, R. Hackl, E. A. Nowadnick, A. F. Kemper, T. P. Devereaux, J.-H. Chu, J. G. Analytis, I. R. Fisher, and L. Degiorgi, Alternative route to charge density wave formation in multiband systems, Proc. Natl. Acad. Sci. USA **110**, 64 (2013).
[12] X. Zhu, Y. Cao, J. Zhang, E. W. Plummer, and J. Guo, Classification of charge density waves based on their nature, Proc. Natl. Acad. Sci. USA **112**, 2367 (2015).

[13] I. Bâldea and M. Bădescu, Quasiregular impurity distribution driven by a charge-density wave, Phys. Rev. B **48**, 8619 (1993).

[14] F. J. Di Salvo, C. H. Chen, R. M. Fleming, J. V. Waszczak, R. G. Dunn, S. A. Sunshine, and J. A. Ibers, Physical and structural properties of the new layered compounds Ta_2NiS_5 and Ta_2NiSe_5, J. Less Common Met. **116**, 51 (1986).

[15] R. M. Fleming, S. A. Sunshine, C. H. Chen, L. F. Schneemeyer, and J. V. Waszczak, Defect-inhibited incommensurate distortion in Ta_2NiSe_7, Phys. Rev. B **42**, 4954 (1990).

[16] S. Siddique *et al.*, Emerging two-dimensional tellurides, Mater. Today **51**, 402 (2021).

[17] K. Yumigeta, Y. Qin, H. Li, M. Blei, Y. Attarde, C. Kopas, and S. Tongay, Advances in rare-earth tritelluride quantum materials: Structure, properties, and synthesis, Adv. Sci. **8**, 2004762 (2021).

[18] E. DiMasi, M. C. Aronson, J. F. Mansfield, B. Foran, and S. Lee, Chemical pressure and charge-density waves in rare-earth tritellurides, Phys. Rev. B **52**, 14516 (1995).

[19] Y. Wang *et al.*, Axial Higgs mode detected by quantum pathway interference in RTe_3, Nature (London) **606**, 896 (2022).

[20] H. Yao, J. A. Robertson, E.-A. Kim, and S. A. Kivelson, Theory of stripes in quasi-two-dimensional rare-earth tellurides, Phys. Rev. B **74**, 245126 (2006).

[21] N. Ru, C. L. Condron, G. Y. Margulis, K. Y. Shin, J. Laverock, S. B. Dugdale, M. F. Toney, and I. R. Fisher, Effect of chemical pressure on the charge density wave transition in rare-earth tritellurides RTe_3, Phys. Rev. B **77**, 035114 (2008).

[22] J. A. W. Straquadine, M. S. Ikeda, and I. R. Fisher, Evidence for realignment of the charge density wave state in $ErTe_3$ and $TmTe_3$ under uniaxial stress via elastocaloric and elastoresistivity measurements, Phys. Rev. X **12**, 021046 (2022).

[23] A. Fang, J. A. W. Straquadine, I. R. Fisher, S. A. Kivelson, and A. Kapitulnik, Disorder-induced suppression of charge density wave order: STM study of Pd-intercalated $ErTe_3$, Phys. Rev. B **100**, 235446 (2019).

[24] J. A. W. Straquadine, F. Weber, S. Rosenkranz, A. H. Said, and I. R. Fisher, Suppression of charge density wave order by disorder in Pd-intercalated $ErTe_3$, Phys. Rev. B **99**, 235138 (2019).

[25] K. Mallayya, J. Straquadine, M. J. Krogstad, M. D. Bachmann, A. G. Singh, R. Osborn, S. Rosenkranz, I. R. Fisher, and E.-A. Kim, Bragg glass signatures in Pd_xErTe_3 with x-ray diffraction temperature clustering, Nat. Phys. **20**, 822 (2024).

[26] See Supplemental Material at http://link.aps.org/supplemental/10.1103/PhysRevB.110.014111 for additional details on experimental methods, quantitative analysis of electron diffraction patterns and 4D-STEM data, machine learning on 4D-STEM data, and videos showing temperature evolution of CDW in $ErTe_3$, which includes Refs. [27–38].

[27] B. H. Savitzky *et al.*, Image registration of low signal-to-noise cryo-STEM Data, Ultramicroscopy **191**, 56 (2018).

[28] B. H. Goodge, E. Bianco, N. Schnitzer, H. W. Zandbergen, and L. F. Kourkoutis, Atomic-resolution cryo-STEM across continuously variable temperatures, Microsc. Microanal. **26**, 439 (2020).

[29] R. Sundararaman, K. Letchworth-Weaver, K. A. Schwarz, D. Gunceler, Y. Ozhabes, and T. A. Arias, JDFTx: Software for joint density-functional theory, SoftwareX **6**, 278 (2017).

[30] K. F. Garrity, J. W. Bennett, K. M. Rabe, and D. Vanderbilt, Pseudopotentials for high-throughput DFT calculations, Comput. Mater. Sci. **81**, 446 (2014).

[31] J. P. Perdew, K. Burke, and M. Ernzerhof, Generalized gradient approximation made simple, Phys Rev. Lett. **77**, 3865 (1996).

[32] S. Grimme, J. Antony, S. Ehrlich, and H. Krieg, A consistent and accurate *ab initio* parametrization of density functional dispersion correction (DFT-D) for the 94 elements H-Pu, J. Chem. Phys. **132**, 154104 (2010).

[33] The abTEM code: Transmission electron microscopy from first principles, Open Res. Eur. **1** (2021).

[34] Y.-T. Shao, R. Yuan, H.-W. Hsiao, Q. Yang, Y. Hu, and J.-M. Zuo, Cepstral scanning transmission electron microscopy imaging of severe lattice distortions, Ultramicroscopy **231**, 113252 (2021).

[35] D. D. Lee and H. S. Seung, Learning the parts of objects by non-negative matrix factorization, Nature (London) **401**, 6755 (1999).

[36] D. Lee and H. S. Seung, Algorithms for non-negative matrix factorization, *Advances in Neural Information Processing Systems 13* (MIT Press, Cambridge, MA, 2000).

[37] C.-J. Hsieh and I. S. Dhillon, Fast coordinate descent methods with variable selection for non-negative matrix factorization, in *Proceedings of the 17th ACM SIGKDD International Conference on Knowledge Discovery and Data Mining* (ACM, San Diego, CA, 2011), pp. 1064–1072.

[38] F. Pedregosa *et al.*, Scikit-learn: Machine learning in Python, J. Mach. Learn. Res. **12**, 2825 (2011).

[39] C. Ophus, Four-dimensional scanning transmission electron microscopy (4D-STEM): From scanning nanodiffraction to ptychography and beyond, Microsc. Microanal. **25**, 563 (2019).

[40] S. Amelinckx, *The Direct Observations of Dislocations* (Academic Press, New York, 1964).

[41] L. Fu, A. M. Kraft, B. Sharma, M. Singh, P. Walmsley, I. R. Fisher, and M. C. Boyer, Multiple charge density wave states at the surface of $TbTe_3$, Phys. Rev. B **94**, 205101 (2016).

[42] A. Kogar *et al.*, Light-induced charge density wave in $LaTe_3$, Nat. Phys. **16**, 159 (2020).

[43] C. Gammer, V. Burak Ozdol, C. H. Liebscher, and A. M. Minor, Diffraction contrast imaging using virtual apertures, Ultramicroscopy **155**, 1 (2015).

[44] J. L. Hart *et al.*, Emergent layer stacking arrangements in *c*-axis confined $MoTe_2$, Nat. Commun. **14**, 1 (2023).

[45] P. A. Lee and T. M. Rice, Electric field depinning of charge density waves, Phys. Rev. B **19**, 3970 (1979).

[46] B. H. Goodge, I. El Baggari, S. S. Hong, Z. Wang, D. G. Schlom, H. Y. Hwang, and L. F. Kourkoutis, Disentangling coexisting structural order through phase lock-in analysis of atomic-resolution STEM data, Microsc. Microanal. **28**, 404 (2022).

[47] A. A. Sinchenko, P. Lejay, O. Leynaud, and P. Monceau, Unidirectional charge-density-wave sliding in two-dimensional rare-earth tritellurides, Solid State Commun. **188**, 67 (2014).

[48] A. V. Frolov, A. P. Orlov, A. A. Sinchenko, and P. Monceau, Features of pinning of a charge-density wave in quasi-two-dimensional compounds, JETP Lett. **109**, 203 (2019).

[49] Y. Yu and S. A. Kivelson, Fragile superconductivity in the presence of weakly disordered charge density waves, Phys. Rev. B **99**, 144513 (2019).